# Complete Phenomenological Model for Projectile-Breakup Reactions
## (Report to the 2nd RCM of the FENDL-3 CRP)

Constance Kalbach Walker

*Triangle Universities Nuclear Laboratory, Duke University, Durham NC 27701, USA*

(Dated: 18 March 2010)

A phenomenological model for light-projectile breakup has been developed using data for deuteron, $^3$He, and $\alpha$-particle induced reactions. Global systematics for the centroid energies, peak widths, angular distributions, and the target-mass-number dependence of the absolute breakup cross section were reported for the 1st Research Coordination Meeting. Since then, the angular distribution systematics have been significantly revised, and the incident-energy dependence of the cross section for each breakup channel has been determined. A small computer code implements the model and is being used for comparisons with experimental double differential cross sections. Comparisons are presented for deuteron breakup at 15 and 56 MeV. This code will eventually become a subroutine in larger reactions codes, thus making possible the final benchmarking of these codes for complex-particle-induced reactions, in particular with regard to the initial particle-hole configuration used in the exciton preequilibrium model.

## I. INTRODUCTION

One of the important goals of the FENDL-3 development project is the inclusion of deuteron-induced reactions in the data library. This will rely heavily on reaction model calculations, but general reaction model codes typically lack a model for the deuteron-breakup mechanism, which makes important contributions at almost all incident energies. The development of a robust projectile-breakup model is, therefore, an important priority for the FENDL-3 Coordinated Research Project.

Projectile breakup is here defined as the emission of a projectile fragment with a fairly narrow energy distribution peaked at an emission energy corresponding to the projectile velocity. These fragments are emitted with an angular distribution that is more sharply peaked toward forward angles than the surrounding and underlying cross section. When the undetected fragment interacts with the target nucleus, it forms a composite system that will then undergo energy equilibration. Particle emission occuring during and after that equilibration will need to be included in reaction model codes.

The question of projectile breakup, however, extends beyond deuterons. The breakup mechanism also makes significant contributions for reactions induced by $^3$He ions and, at sufficiently high incident energies, by $\alpha$-particles. Until a model for this mechanism is included in preequilibrium-model reaction codes, it is impossible to finalize the benchmarking of these codes for complex-particle-induced reactions. In particular, a definitive assignment of the initial particle-hole configuration in the exciton model cannot be made for complex-particle projectiles, because projectile breakup is expected to significantly reduce the amount of the total reaction cross section going into the main exciton-model equilibration calculations.

Given the importance of the projectile-breakup mechanism, both from a basic physics perspective and for energy applications, a phenomenological breakup model has been developed. It is designed for inclusion in the next release of the TUNL preequilibrium reaction code PRECO and in larger, more comprehensive Hauser-Feshbach model codes such as GNASH and TALYS.

## II. DATABASE

The model reported here was developed based on data for deuteron, $^3$He, and $\alpha$-particle breakup. This yields a more robust and global model than one developed for deuteron breakup alone, because it uncovers the dependence of the breakup reaction on the energy required to separate the projectile into its constituent fragments. Continuum energy spectra measured at a variety of forward angles in a given reaction have been collected from the literature. All of the detected fragments are charged particles, so it will be assumed that neutron fragments follow generally the same systematics as proton fragments, except, of course, that there will be no Coulomb barrier in the exit channel. The data used are summarized in Table I. Other data at lower incident energies are available for $^3$He and $\alpha$-particle projectiles, but the breakup peaks, when present, are not distinct enough to be used in this study.

In order to develop a model for projectile breakup, the breakup peak must be differentiated from the underlying continuum cross section. This involves drawing a "background" underneath the obvious breakup peak, where the background is typically the usual preequilibrium cross section. This separation process was carried out for all of the

TABLE I: Literature data used in developing the projectile breakup model.

| Proj. | $E_{\text{inc}}$ (MeV) | Targets | Ejectile | Angles | Ref. |
|---|---|---|---|---|---|
| d | 14.8 | Al, Cu , Zr, Cd, Pt | p | 12°-85° | [1] |
|  | 14.8 | 11 others | p | 30° | [1] |
|  | 15.0 | $^{62}$Ni, Ta | p | 23°-120° | [2] |
|  | 25.5 | Al, $^{62}$Ni, Nb, $^{119}$Sn, Ta | p | 20°-120° | [3] |
|  | 27.5 | $^{57}$Fe, $^{116}$Sn | p | 20°-90° | [4] |
|  | 56 | Al, $^{58}$Ni, $^{90}$Zr, $^{118}$Sn, Bi | p | 9.5°-30° | [5] |
|  | 56 | 9 others | p | 9.5° | [5] |
|  | 70 | $^{90}$Zr, $^{208}$Pb, $^{232}$Th | p | 20°-90° | [6] |
|  | 80 | Al, $^{58}$Ni | p | 20°-90° | [6] |
| $^3$He | 70, 90, 110 | $^{90}$Zr | d | 13°-30° | [7] |
|  | 70 | 6 others | d | 13° | [7] |
|  | 90 | 11 others | d | 13° | [7] |
|  | 70, 90 | $^{90}$Zr | p | 13°-40° | [7] |
|  | 130 | Al, Co, Nb, Au | d | 7.5°-21° | [8] |
| $\alpha$ | 80 | Al, $^{58}$Ni, $^{90}$Zr | p,d | 6°-26° | [9] |
|  | 80 | Al | t,$^3$He | 6°-26° | [9] |
|  | 140 | Bi | $^3$He | 13°-20° | [10] |
|  | 160 | Al, $^{58}$Ni, $^{90}$Zr, Bi | p,d,t,$^3$He | 6°-26° | [9] |

spectra analyzed and is the greatest source of uncertainty in the present work. Even the assignment of uncertainties to the quantities extracted from the breakup peaks is a subjective process. Fortunately both the peak energies and their widths appear to be generally independent of the emission angle, so data from more than one angle can sometimes be used, thus reducing uncertainties. All analyses are carried out in the laboratory system.

## III. CENTROID ENERGIES

The simplest estimate of the energy of the breakup peak is that it corresponds to a fragment moving at the projectile velocity, so that $E_0 = E_{\text{inc}} A_b/A_a$, where $A_a$ and $A_b$ are the mass numbers of the projectile and the detected fragment, respectively, and $E_{\text{inc}}$ is the projectile energy in the laboratory system. The actual peak energy can be shifted from this value by Coulomb deceleration in the entrance channel and by Coulomb acceleration in the exit channel. In the case of "dissociative" breakup, where both projectile fragments continue moving forward, the requirement of supplying the projectile's dissociation energy would lower the peak energy, but experimental peak energies for both $^3$He and $\alpha$-particle breakup exclude this as being a dominant mechanism. Instead, they point to "absorptive" breakup, in which the non-observed fragment interacts strongly with the target and the observed fragment is largely a spectator. For incident $\alpha$ particles, this observation is confirmed by coincidence measurements [11], so absorptive breakup is here assumed to be the dominant mechanism. Thus the final expression for the peak energies is

$$E_0 = A_b/A_a \left(E_{\text{inc}} - C_{\text{a}}\right) + C_{\text{b}}, \tag{1}$$

where $C_{\text{a}}$ and $C_{\text{b}}$ are the Coulomb barriers in the entrance and exit channels, respectively. The barrier $C_{\text{a}}$ expressed in MeV is given by

$$C_{\text{a}} = 1.44 Z_{\text{a}} Z_{\text{A}}/D_0, \tag{2}$$

where $Z_{\text{a}}$ and $Z_{\text{A}}$ are the atomic numbers of the projectile and target, respectively. A similar expression applies for $C_{\text{b}}$. Here $D_0$ is the effective target-projectile separation at the point of interaction and is given in femtometers.

Using the experimental peak positions for the heaviest targets (the ones with the largest Coulomb barriers), estimates of the Coulomb shifts in the peak positions have been used to extract estimates for $D_0$. These results have been fit with the formula

$$D_0 = r_0 A^{1/3} + 1.2 \text{ fm}, \tag{3}$$

where $r_0$ is an effective radius parameter that depends only on the incident energy, and where the constant 1.2 fm should represent the size of the projectile. Here $A$ is the target mass number, and $r_0$, like $D_0$, is given in femtometers. Values of $r_0 = (D_0 - 1.2\text{ fm})/A^{1/3}$ were extracted for each breakup channel and incident energy for which adequate data were available, and the results are shown in Fig. 1. The results for the three projectile types seem to generally follow a common trend with incident energy and can be adequately reproduced by the formula

$$r_0 = 1.2 + \frac{5}{1 + \exp(E_{\text{inc}}/30)}, \tag{4}$$

where the projectile energy $E_{\text{inc}}$ is assumed to be given in MeV. The curve in Fig. 1 corresponds to this result. It is assumed that this formula will apply to lighter targets as well, since the data uncertainties do not allow the $Z$-dependence of $r_0$ to be probed.
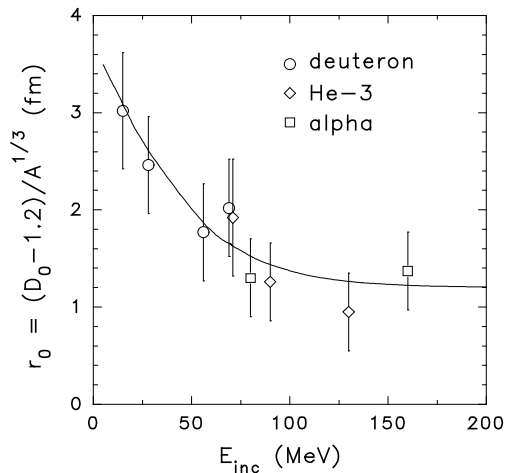


FIG. 1: Effective radius parameter for projectile breakup. The points show the values inferred from the Coulomb shifts in the energies of the breakup peaks in literature data for the indicated projectiles. In each case the results from the heaviest available target were chosen, since these have the largest energy shifts. The solid curve shows the fitted dependence given by Eq. (4). Its asymptotic value is 1.2 fm.

The systematic peak energies for $(d,p)$, $(^3\text{He},d)$, and $(^3\text{He},p)$ breakup obtained from Eqs. (1)-(4) are shown in Fig. 2 along with the experimental values. Figure 3 shows the same quantities for $\alpha$-particle breakup.
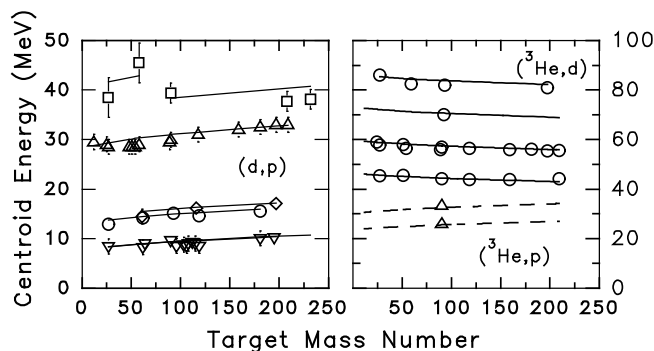


FIG. 2: Experimental peak energies for $(d,p)$, $(^3\text{He},d)$, and $(^3\text{He},p)$ breakup. The points show the values extracted from the data, while the lines represent the systematic values obtained from Eq. (1). The incident energies for $(d,p)$ are (from the top curve to the bottom) 80, 70, 56, 27.5, 25.5, and 15 MeV. For $(^3\text{He},d)$, the incident energies are 130, 110, 90, and 70 MeV, while for $(^3\text{He},p)$ they are 90 and 70 MeV.
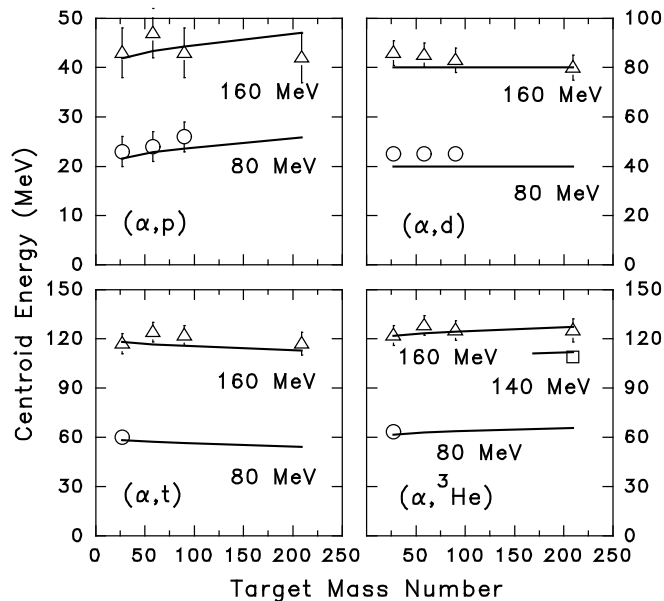
FIG. 3: Experimental peak energies for $(\alpha,p)$, $(\alpha,d)$, $(\alpha,t)$, and $(\alpha,^3\text{He})$ breakup at the indicated incident energies. The points show the values extracted from the data, while the lines represent the systematic values obtained from Eq. (1).

## IV. PEAK SHAPES AND WIDTHS

### A. Basic systematics

The breakup peaks are assumed to have a Gaussian shape so that the normalized energy distribution is

$$P_E(\varepsilon) = \frac{1}{\sqrt{2\pi}w} \exp\left[-\frac{(E - E_0)^2}{2w^2}\right],\tag{5}$$

where $w$ is the peak width, $E$ is the energy of the observed breakup fragment, and $P_E(E)$ integrates to unity.

The full width at half maximum (FWHM) of the breakup peaks is denoted as $F = 2.35w$. Values for $F$ were estimated from spectra in the database. They appear to be largely independent of emission angle and only weakly dependent on target mass number. A workable empirical formula for this width, given in MeV, is

$$F = 62\left[1 - \frac{1}{\exp(E_{\text{inc}}/173)}\right]\left[1 - \frac{A}{155(S_{\text{a,b}})^2}\right] - 3\,\Theta(A_a - A_b - 1.5),\tag{6}$$

where $S_{\text{a,b}}$ is the energy required to separate the projectile into the observed fragment $b$ and its complement, and $\Theta$ is the Heaviside step function, which is zero for a negative argument and one for a positive argument. Both $E_{\text{inc}}$ and $S_{\text{a,b}}$ are given in MeV. The last term in Eq. (6) lowers the FWHM for $(^3\text{He},p)$, $(\alpha,p)$ and $(\alpha,d)$ breakup relative to the channels where only a single nucleon is absorbed by the target. This difference between channels with $A_{\text{b}} = A_{\text{a}} - 1$ and those with $A_{\text{b}} < A_{\text{a}} - 1$ was unexpected but appears again in the angular distribution systematics discussed below. A comparison of widths obtained from Eq. (6) with the experimental values for $(d,p)$, $(^3\text{He},d)$, and $(^3\text{He},p)$ breakup reactions is shown in Fig. 4. Similar results for $\alpha$-particle breakup are shown in Fig. 5. Agreement is generally good except for $(\alpha,^3\text{He})$. The discrepancies between experiment and the base systematics in the $(\alpha,^3\text{He})$ case are due to the effect of the kinematic limit on the fragment energy, which needs to be taken into account.

In fact, the peak shapes, widths, and, in extreme cases, even their positions can all be modified by either the Coulomb barrier or the maximum-energy cutoff in the spectrum due to energy conservation. These effects have not been observed in deuteron breakup, but the maximum-energy-cutoff effect plays a role in $(\alpha,t)$ as well as $(\alpha,^3\text{He})$ breakup, as can be seen in the smaller empirical widths in Fig. 5. Both effects have been included in the model, as discussed in the next section.
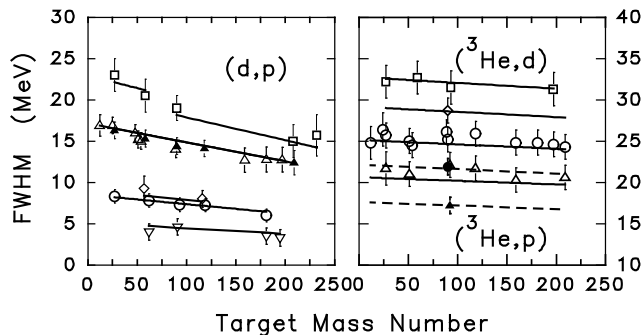
FIG. 4: FWHM for $(d,p)$ and $(^3\text{He},d)$ breakup peaks. The points show the experimental values extracted from data in the literature, while the lines are obtained from Eq. (6). The incident energies for the $(d,p)$ curves are (from top to bottom) 80, 70, 56, 27.5, 25.5, and 14.8 MeV. At 56 MeV, the solid points are those for the targets where data are available at a number of different detection angles. The open points show the results at 30 degrees. The incident energies for the $(^3\text{He},d)$ curves are 130, 110, 90, and 70 MeV. There are also empirical values for $(^3\text{He},p)$ breakup on $^{90}\text{Zr}$ at 90 and 70 MeV. These are given by the solid data points and the dashed calculated curves.
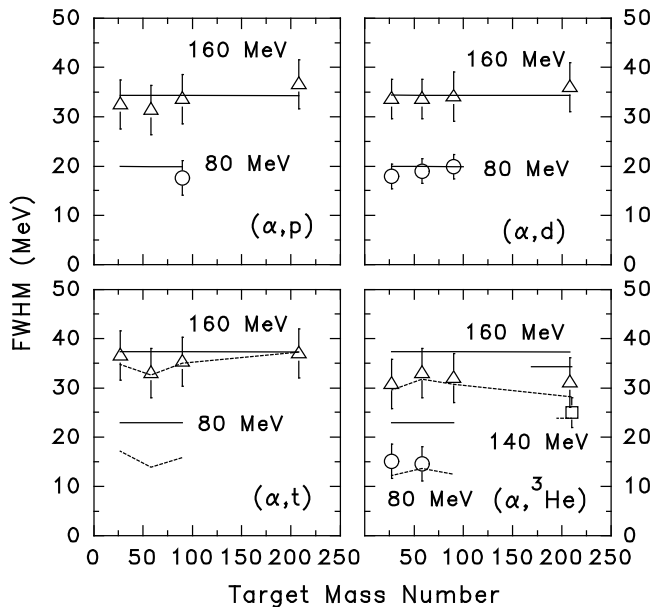


FIG. 5: FWHM for $\alpha$-particle breakup peaks. The points show the experimental values extracted from data in the literature, the solid lines are obtained from the base systematics of Eq. (6), and the dotted lines include the effects of the kinematic limit on the maximum fragment energy according to Eq. (7). The calculated widths are shown for $(\alpha,t)$ breakup at 80 MeV even though there are no experimental values.

## B. Modifications from the Maximum-Energy Cutoff and the Coulomb Barrier

Some of the $(\alpha,t)$ and $(\alpha,^3\text{He})$ breakup peaks appear to be assymetric, with the higher emission energy side being narrower. This is due to restrictions placed on the peak width by the kinematic limit on the energy of the observed fragment. This effect can be included in the model by leaving the peak in its normal position and using different widths for the two halves of the Gaussian distribution. If $E_{\max}$ is the maximum energy kinematically allowed and $H = F/2$ is the half width at half maximum from the base systematics, then the full width at half maximum becomes

$$F_{\text{eff}} = H + \min\left[H, 0.6(E_{\max} - E_0)\right] \tag{7}$$

where the factor of 0.6 is an empirical estimate. The resulting FWHM values for the current data set are different from the base systematics only for $(\alpha,t)$ and $(\alpha,^3\text{He})$ breakup, and the reduced values from Eq. (7) are shown as

dashed curves in Fig. 5.

In more extreme cases than those observed in the current database, it is possible to have $E_{max} < E_0$, so that $E_{max}$ becomes the new peak energy. The results for the observed asymmetric peaks have been extended to this cases in the interest of arriving at a global model. Two additional ranges of $E_{max}$ are needed. In general, the peak shape for each range of $E_{max}$ is characterized by the half widths at half maximum, $H_-$ and $H_+$, for the half Gaussians lying below and above the peak energy $E_{pk}$, respectively, so that the effective FWHM becomes

$$F_{eff} = H_- + H_+ \tag{8}$$

The full prescription is summarized in Table II, where the results for the peak energy can be summarized as $E_{pk} = \min(E_0, \epsilon_{max})$.

TABLE II: Equations for the half widths at half maximum for the lower and upper half Gaussians of the breakup fragment energy distribution.

| Range | $H_-$ | $H_+$ | $E_{pk}$ |
|---|---|---|---|
| $E_0 + 1.67H \leq E_{max}$ | $H$ | $H$ | $E_0$ |
| $E_0 \leq E_{max} < E_0 + 1.67H$ | $H$ | $0.6(E_{max} - E_0)$ | $E_0$ |
| $E_0 - 1.67H \leq E_{max} < E_0$ | $H - 0.6(E_0 - E_{max})$ | $0$ | $E_{max}$ |
| $E_{max} < E_0 - 1.67H$ | $0$ | $0$ | |

Finally, there is the question of the exit-channel Coulomb barrier. If it is high enough relative to the energy of the breakup peak, then it could distort the peak shape, so that the equation for the Gaussian should be multiplied by a barrier penetrability factor:

$$T_E(E) = \left[ 1 + \exp\left( \frac{(C_b - E)}{C_b/3} \right) \right]^{-1} \tag{9}$$

where $E$ is the energy of the observed fragment. The penetrability factor was not included in the analysis of the data to determine the systematics of the breakup peaks (position, shape or magnitude), nor did it seem to be needed, but it is tentatively included in the model.

The resulting equation for the peak shape is then

$$P_E(\varepsilon) = \frac{1}{\sqrt{2\pi}w} \exp\left[ -\frac{(E - E_{pk})^2}{2(2w_i)^2} \right] T_E(E), \tag{10}$$

where

$$w = w_+ + w_- = \frac{F_{eff}}{2.35}, \tag{11}$$

$$w_+ = \frac{H_+}{2.35} = \frac{1}{2.35} \max\{0, \min[H, 0.6(E_{max} - E_0)]\}, \tag{12}$$

$$w_- = \frac{H_-}{2.35} = \frac{1}{2.35} \max\left(0, \{H - \max[0, 0.6(E_0 - E_{max})]\}\right), \tag{13}$$

$$w_i = \begin{cases} w_- & \text{for} \quad E \leq E_{pk} \\ w_+ & \text{for} \quad E > E_{pk} \end{cases}. \tag{14}$$

In the base case, in which neither the kinematic limit nor the Coulomb barrier distorts the peak shape, the energy integral over the peak shape is clearly unity, from the normalization of the plain Gaussian. When the kinematic limit on the maximum energy of the detected fragment comes into play, the use of $w = w_+ + w_-$ in the pre-exponential of Eq. (10) preserves the normalization to unity for peaks with a finite width. However, the Coulomb penetrability, if it is truly applicable, clearly lowers the breakup cross section.

## V. BREAKUP ANGULAR DISTRIBUTIONS AND $A$-DEPENDENCE OF THE BREAKUP CROSS SECTION

Having established the emission-energy distribution of the breakup peaks, the next step is to describe the angular distribution of the detected fragments. Because this requires having data available at a significant number of angles for a given target as well as for a variety of breakup channels, incident energies and target masses, the database is more limited and the derived systematics are more tentative. Future revisions will surely be necessary.

## A. Base Systematics

For a given breakup channel and incident energy, the data from a variety of targets show that at each emission angle the breakup cross section is approximately proportional to $(D_0)^2$. Thus the data from different targets can be divided by $(D_0)^2$ and plotted as a function of emission angle in the laboratory system in order to study the average angular distribution systematics.

With the exception of the $(d,p)$ breakup peaks for targets with $A \geq 90$ at an incident energy of around 15 MeV, the remaining data show an angular distribution that is a negative exponential in the emission angle $\theta$. This is shown for the 56 MeV $(d,p)$ data in Fig. 6. Here the angle-differential cross section has been estimated from the empirical peak height and the systematic FWHM rather than by integrating the individual peaks.
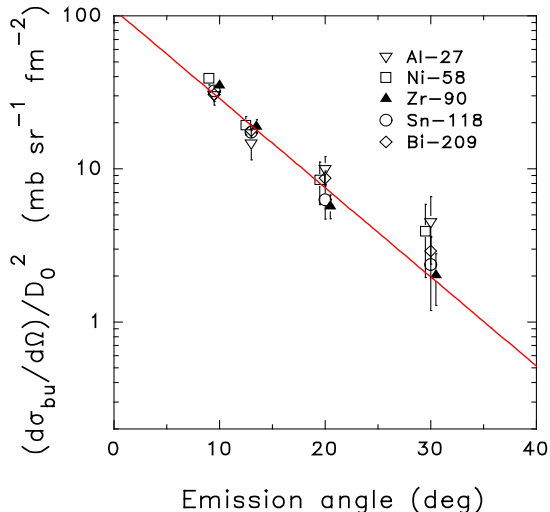


FIG. 6: Normalized angular distributions for $(d,p)$ breakup at 56 MeV. The points show the experimental breakup cross sections divided by $(D_0)^2$ as a function of angle, while the line shows the best fit with an exponential in the emission angle.

The points in this and similar plots for different breakup channels and different incident energies were fit with a dependence of the form

$$\frac{d\sigma_{\rm bu}(\theta)}{d\Omega}\frac{1}{(D_0)^2} = Ke^{-a_{\rm bu}\theta}. \tag{15}$$

where $K$ and $a_{\rm bu}$ were the fitting parameters. The results of this fitting are also shown in Fig. 6. The values of the angular distribution slope $a_{\rm bu}$ were then studied to look for systematics. Here again, as was the case for the peak widths, a difference seems to emerge between the breakup channels with $A_{\rm b} = A_{\rm a} - 1$ and those with $A_{\rm b} < A_{\rm a} - 1$. In the latter case, the angular distribution slope appears to be independent of incident and emission energy. On the other hand, for $A_{\rm b} = A_{\rm a} - 1$, the results show a definite energy dependence which can be parameterized in terms of either the incident energy or the peak energy. The parameterization in terms of the peak energy, $E_{\rm pk} = E_0$, gives a slightly better fit and is more consistent with the systematics for the underlying continuum angular distributions, which are likewise expressed as a function of the emission energy. The empirical average slope parameters $a_{\rm bu}$ are shown as a function of the average peak energy $\langle E_0 \rangle$ in Fig. 7. The error bars in the figure reflect only the uncertainty in the slope values assigned by the fitting program and do not include uncertainties due to background subtraction in extracting the peak heights from the experimental spectra or uncertainties in the values of $(D_0)^2$. A linear dependence of $a_{\rm bu}$ on the peak energy was tried first and was reported to the first FENDL-3 RCM, but data comparison with the full breakup model showed that it did not to give an accurate enough description of the data. The fitted slope parameters are given in $\mathrm{rad}^{-1}$ and now follow the relations

$$a_{\rm bu} = \begin{cases} 4A_{\rm b} + Z_{\rm b} - 2 + 0.029E_0 + \frac{7.6}{A_{\rm a}}\left[1 + \exp\left\{(12S_{\rm ab} - E_0)/0.84S_{\rm ab}\right\}\right]^{-1} & \text{for } A_{\rm b} = A_{\rm a} - 1 \\ 4.7 + A_{\rm b} & \text{for } A_{\rm b} < A_{\rm a} - 1 \end{cases}. \tag{16}$$

The results from these systematics are also shown in Fig. 7 and reproduce the general trends of the empirical values. Again, however, it must be emphasized that both the form and the parameter values were chosen to give a single, global mathematical description of current data and depend on physically reasonable reaction variables, but they must still be regarded as tentative and even somewhat arbitrary.
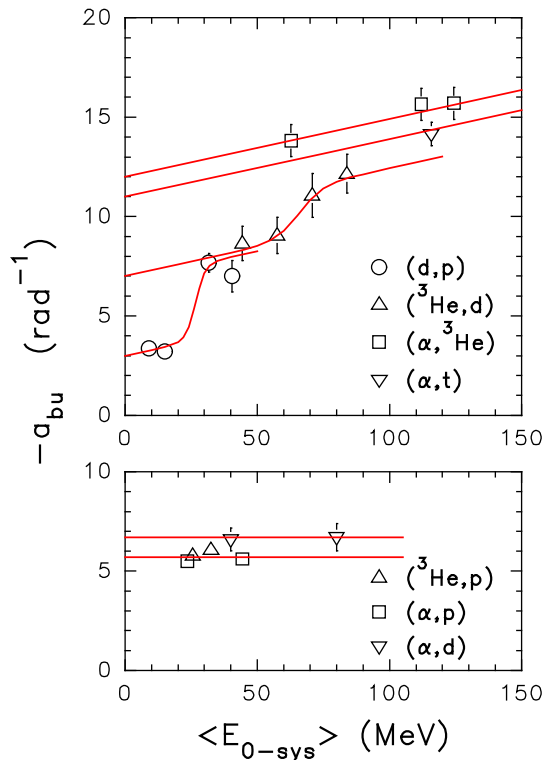
FIG. 7: Empirical values for the breakup-angular-distribution slope parameter $a_{bu}$ as a function of the average centroid energy of the targets for which angular distributions were determined. The lines show the systematics given by Eq. (16).

## B.   Coulomb Dip at Forward Angles

For $(d,p)$ breakup at around 15 MeV, the data for the heavier targets show that the angular distributions are low at forward angles, gradually increase, and then at higher angles begin to follow the normal exponential falloff with $\theta$. The size of the dip at forward angles is correlated with the size of the Coulomb barrier relative to the incident energy. The dip has been parameterized as an angular penetrability factor multiplying the basic angular distribution of Eq. (15). The forward-angle dip does not seem to reduce the breakup cross section but simply to redistribute it to larger angles. Thus, in the presence of such a dip, the probability of emission at a particular angle $\theta$ becomes

$$P_\theta(\theta) = \frac{(a_{bu})^2 + 1}{2\pi} e^{-a_{bu}\theta} \, T_\theta(\theta), \tag{17}$$

$$T_\theta(\theta) = \frac{1}{I_{eff}} \left[ 1 + \exp\left(\frac{\theta_0 - \theta}{w_\theta}\right) \right]^{-1}, \tag{18}$$

where the normalization $\left[(a_{bu})^2 + 1\right]/2\pi$ was included in the constant $K$ in Eq. (15). Here $\theta_0$ characterizes the angular "barrier" and $w_\theta$ determines its width. Both are given in units of radians. The quantity $I_{eff}$ keeps the angle integral of $P_\theta(\theta)$ normalized to unity. Values of $\theta_0$ can be estimated for the heavier targets in $(d,p)$ breakup at 14.8 and 15 MeV, and upper limits on $\theta_0$ can be estimated for the lighter targets, where no dip is seen. For $(d,p)$ breakup at higher energies and for other breakup channels, the systematics of $\theta_0$ are not well determined, so the present results must be regarded as very tentative. For example, for $(^3\mathrm{He},d)$ breakup at 70 and 90 MeV, angular distributions are available only for $^{90}\mathrm{Zr}$.

On the other hand, double-differential cross sections for these and other breakup channels are sometimes available for a series of targets at a single forward angle, and deviations for heavy targets from the usual $(D_0)^2$ dependence can provide evidence of a forward-angle dip. A rough estimate of $\theta_0$ in such situations has been made by assuming that $w_\theta = \min(\theta_0/3, 0.1)$, as indicated by the $(d,p)$ breakup trends at 15 MeV, and that the angle-integrated cross section is proportional to $(D_0)^2$. Calculations of the peak height at the experimental angle were carried out for different values of $\theta_0$, and the factors required to normalize the calculated peak heights to the experimental values for a series

of targets were estimated. For each breakup channel and incident energy, the required normalization factors were plotted as a function of $\theta_0$ with the results for all of the targets on a single plot. The goal was to find a single normalization factor for each reaction channel and incident energy that corresponds to $\theta_0$ values that vary smoothly in going from light to heavy targets and predicts at most a small dip for the lighter targets that show a peak cross section proportional to $D_0$ when no angular barrier is used in the calculations.

This kind of exercise was first carried out for $(d,p)$ breakup at around 15 MeV, where angular distributions are available, to see how the method works. It was then applied to other reaction channels and incident energies where sufficient data were available. These are $(d,p)$ at 56 MeV and $(\alpha,d)$ at 160 MeV, where only upper limits on $\theta_0$ are obtained, and $(^3\mathrm{He},d)$ at 70 and 90 MeV,. The empirical values of $\theta_0$ and the upper limits, given in radians, are shown in Fig. 8. They have been fit with the relationship
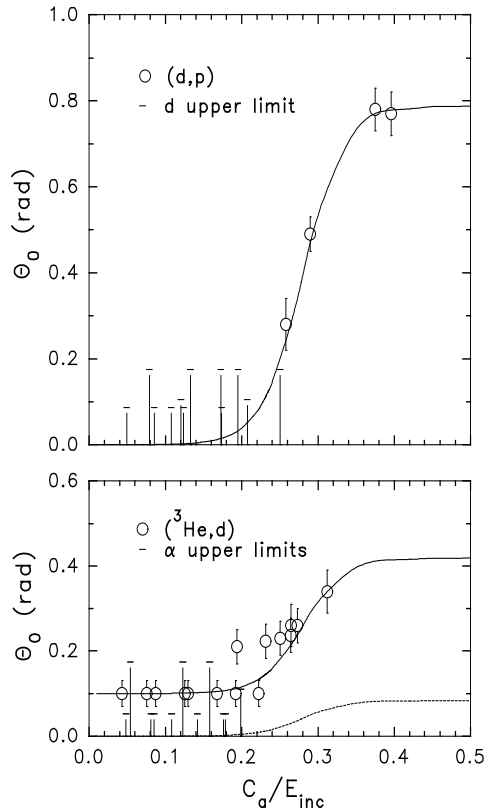


FIG. 8: Systematics of the critical angle $\theta_0$ characterizing the forward-angle Coulomb dip in the angular distributions for the projectile-breakup cross section. The points show values extracted from the data, and the dashes with negative error bars indicate upper limits. The lines show the systematics given by Eq. (19)

$$\theta_0 = 0.1\,|Z_\mathrm{a} - N_\mathrm{a}| + \frac{1.75}{S_\mathrm{ab}}\left[1 + \exp\left(\frac{0.28 - C_\mathrm{a}/E_\mathrm{inc}}{0.027}\right)\right]^{-1}, \tag{19}$$

where the first term was determined largely from the low $C_\mathrm{a}/E_\mathrm{inc}$ values for $(^3\mathrm{He},d)$ breakup along with the upper limits for $(d,p)$ breakup and $\alpha$-particle breakup. The other numerical constants were the three fit parameters determined from $(d,p)$ breakup. The $1/S_\mathrm{ab}$ dependence assumed in order to give a reasonable upper limit for $(^3\mathrm{He},d)$ breakup. The values obtained from this equation are also shown in the figure. As previously noted, the width of the angular barrier has been estimated empirically from $(d,p)$ breakup at 14.8 to 15 MeV and is given as

$$w_\theta = \min(0.1, \theta_0/3). \tag{20}$$

The normalization $I_\mathrm{eff}$ in Eq. (18) is defined approximately in terms of $I_0$, the factor for normalizing the integral when $w_\theta = 0$ (the sharp cutoff limit), and of the angle $\theta_\mathrm{eff}$, which, in the $w_\theta = 0$ limit would give the same integral

as the real distribution with a finite $w_\theta$. These quantities are given by the relations

$$I_0 = e^{-a_{\mathrm{bu}}\theta_0} \left(\cos\theta_0 + a_{\mathrm{bu}}\sin\theta_0\right), \tag{21}$$

$$\theta_{\mathrm{eff}} = \theta_0 + 2.35\, a_{\mathrm{bu}} \left(w_\theta\right)^2 \left(I_0 - 0.62\right), \tag{22}$$

$$I_{\mathrm{eff}} = e^{-a_{\mathrm{bu}}\theta_{\mathrm{eff}}} \left(\cos\theta_{\mathrm{eff}} + a_{\mathrm{bu}}\sin\theta_{\mathrm{eff}}\right). \tag{23}$$

The results obtained from Eqs. (17)-(23) for $(d,p)$ breakup at 14.8 and 15 MeV are shown in Fig. 9 along with the corresponding data. The overall normalization was chosen to give a good fit to the nickel and copper data; it was not adjusted for the individual targets. If the same equations are applied for $(d,p)$ breakup at 25.5 MeV, the resulting
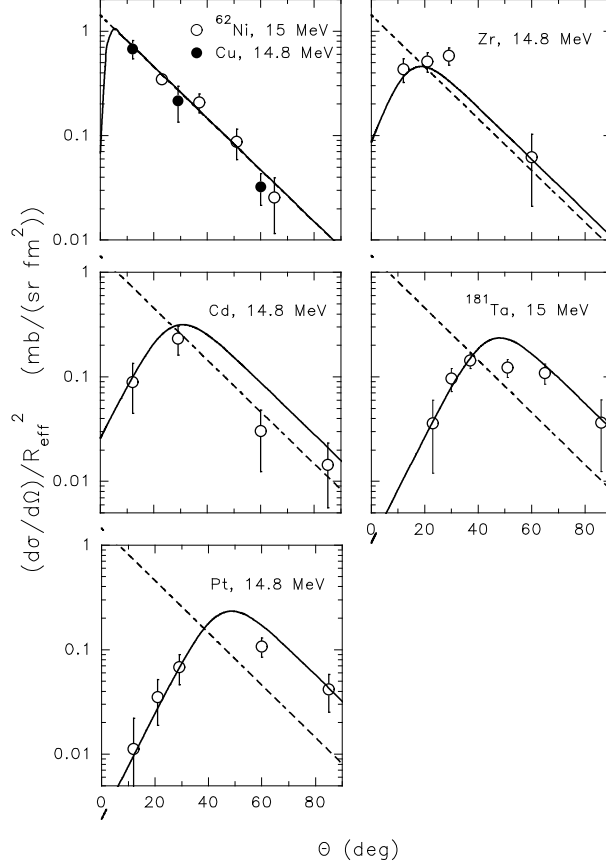


FIG. 9: Angular distributions for the $(d,p)$ breakup peaks at incident energies of 14.8 and 15.0 MeV. The points show the results obtained from experimental spectra, the dashed curves show the results from Eq. (15), and the solid curves are obtained when the angular barriers are included using Eq. (17). All of the data at 14.8 MeV were measured on targets with natural isotopic abundance.

forward angle dip occurs at angles smaller than those for which data are available, and the dip has no significant effect in reproducing the experimental angular distributions.

The results here for the Coulomb dip in the angular distributions must be regarded as very preliminary, since they have been derived and tested mainly for $(d,p)$ breakup at around 15 MeV.

## VI.   TOTAL BREAKUP CROSS SECTION

It has already been observed that the absolute cross section for projectile breakup at each emission energy and angle is proportional to $(D_0)^2$, the effective target-projectile separation distance at the interaction point, but the dependence on incident energy and on the specific breakup channel has yet to be determined. This can be obtained using the normalization constants from fitting the calculated angle-differential cross sections to the measured ones, using the measured peak heights and assuming the systematic values of the FWHM, as was done for the angular

distributions. Dividing out the $D_0$ dependence, an average normalization constant for each breakup channel and incident energy can be obtained. These are shown in Fig. 10. Here the data from the database of Table I have been supplemented with three additional crude points estimated: $^{61}$Ni($^3$He,$p$) and ($^3$He,$p$) at 25.6 MeV [13] and from $^{nat}$Al and $^{nat}$Zr($\alpha$,$n$) at 140 MeV [14], which yield a single point in the figure. It should be noted, however, that these
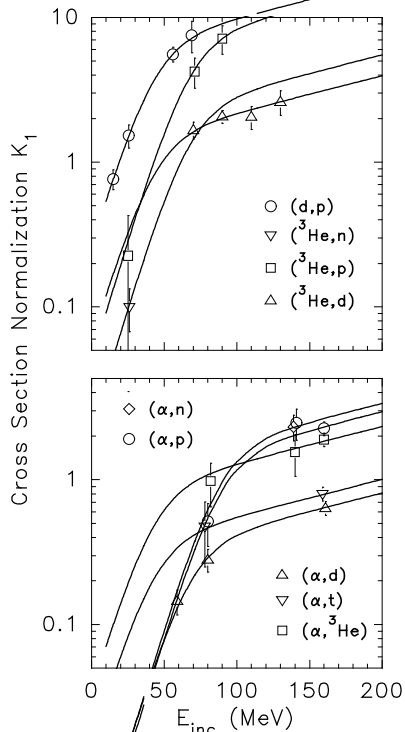


FIG. 10: Average normalization factors $\sigma_{ab}(E_{inc})/(D_0)^2$ for the breakup peaks for the indicated breakup channels as a function of the incident projectile energy. The points show the results obtained from the experimental spectra, and the curves are obtained from Eq. (24).

normalization factors are strongly dependent on the angular distribution systematics, especially for those reactions in which the angular distribution falls off most rapidly with angle. Changing either the slope parameter or $\theta_0$ can significantly change the normalization required. Again, these results should be regarded as tentative.

The most startling observation from Fig. 10 is that for each reaction channel where the data extend to high enough incident energies—($^3$He,$d$), ($\alpha$,$t$), and ($\alpha$,$^3$He)—the breakup cross section at the higher energies seems to approach the same exponential dependence on the incident energy: This dependence has been fit using the data from these three channels. The results correspond to a dependence $\exp[E_{inc}/(170$ MeV]. At lower incident energies there is an initial barrier to be overcome. Thus the absolute breakup cross section can be written as

$$\sigma_{ab}(E_{inc}) = \mathcal{N}_{ab} \ (D_0)^2 \ \exp\left(\frac{E_{inc}}{170 \text{ MeV}}\right) \ T_{1/2}(E_{inc}). \tag{24}$$

This leaves the absolute channel-specific normalization $\mathcal{N}_{ab}$ and the barrier-penetrability factor $T_{1/2}$ to be determined.

The barrier is characterized by the barrier height (the energy $E_{1/2}$ at which the penetrability $T_{1/2}$ reduces the cross section by a factor of two) and by the barrier width. A global form was sought for the function $T_{1/2}$, but the normalization factors $\mathcal{N}_{ab}$ were varied independently. Fits were performed to the ($d$,$p$), ($^3$He,$p$), ($\alpha$,$p$), and ($\alpha$,$d$) data assuming the asymptotic exponential dependence, while varying the parameters $\mathcal{N}_{ab}$, $T_{1/2}$, and $w_\sigma$, the barrier width. Because the barrier is best determined for the ($d$,$p$) reactions and because the values of the width parameters were similar, the ($d$,$p$) value of $w_\sigma = 14$ MeV was adopted, and the fits were then repeated using this fixed width in order to determine values of $T_{1/2}$. The resulting $T_{1/2}$ values were found to vary as $(42$ MeV$)(A_a - A_b)^{2/3}$. Fixing this value, fits to all of the breakup channels in Fig. 10 were repeated to extract final values for the parameter $\mathcal{N}_{a,b}$. The curves

in Fig. 10 thus correspond to

$$T_{1/2}(E_{\text{inc}}, S_{\text{ab}}) = \left[1 + \exp\left(\frac{E_{1/2} - E_{\text{inc}}}{14 \text{ MeV}}\right)\right]^{-1}, \tag{25}$$

$$E_{1/2} = 42 \text{ MeV} \ (A_{\text{a}} - A_{\text{b}})^{2/3}, \tag{26}$$

with the $\mathcal{N}_{\text{ab}}$ values contained in Table III.

TABLE III: Normalization constants $\mathcal{N}_{\text{ab}}$ for the breakup cross section in Eq. (24). Values based on only one data point are given in parentheses. The indicated "sister channels" are ones for which no data were available for this analysis and whose normalization constants are assumed to be the same as those of the main channel in that row of the table.

| breakup channel | $\mathcal{N}_{\text{ab}}$ (mb/fm$^2$) | sister channel |
|---|---|---|
| $(d,p)$ | 5.4 | $(d,n)$ |
| $(^3\text{He},n)$ | (1.25) | $(t,p)$ |
| $(^3\text{He},p)$ | 5.0 | $(t,n)$ |
| $(^3\text{He},d)$ | 1.22 | $(t,d)$ |
| $(\alpha,n)$ | (1.07) | |
| $(\alpha,p)$ | 1.15 | |
| $(\alpha,d)$ | 0.32 | |
| $(\alpha,t)$ | 0.31 | |
| $(\alpha,^3\text{He})$ | 0.73 | |

## VII.   COMPARISONS WITH EXPERIMENT

The present model for projectile-breakup reactions was developed to describe average trends over an extended database. In addition, a Gaussian line shape was assumed and was taken to be independent of emission angle, just as the angular distribution is assumed to be independent of the energy of the detected projectile fragment. Therefore it is important to verify that the model's predictions are in reasonable agreement with measured breakup peaks for particular channels at specific incident energies and emission angles. To accomplish this, a short computer program was written to implement the model, calculating both single- and double-differential cross sections. The breakup peaks calculated in the program were compared with experimental spectra at specific angles for sample reactions. To make the comparisons, an estimate of the continuum cross section underlying the breakup peak was added to the calculated breakup cross section. Comparisons have so far been carried out only for $(d,p)$ breakup at 15 and 56 MeV.

### A.   Deuteron breakup at around 15 MeV

For deuteron breakup at around 15 MeV, there are two data sets, both corresponding to the $(d,p)$ channel, as indicated in Table I. The breakup cross section is quite low at this incident energy, making the comparisons difficult. In addition, the $^{181}$Ta data from Ref. [2] was difficult to extract from the published figures because spectra for eight laboratory angles are shown, all as solid lines that cross each other in ambiguous ways above and below the main breakup peaks, thus introducing sizeable errors in estimating the continuum cross section underlying the breakup peak. The data analysis was also complicated by the presence of deuteron breakup on the detector collimator. A correction for this was made in Ref. [2] by assuming that the 16 degree spectrum was all due to this collimator breakup and by subtracting that spectrum, scaled according to the elastic scattering intensity, from the spectra measured at other angles. However, the spectra at 120 and 170 degrees from deuteron breakup on tantalum are quite similar and show a peak at an energy close to the breakup peak. The intensity is much too high for the peaks to be due to breakup on tantalum, which should be negligible at these angles, and the peaks may represent collimator-breakup contamination. Therefore the 170 degree peak was treated as an extra background component. The data from Ref. [1] appears cleaner and the published graphs are easier to read.

Figures 11-14 show comparisons between the calculation+background curves and the data. The agreement, while far from excellent, is reasonable given the low breakup cross section and the difficulties in estimating the underlying
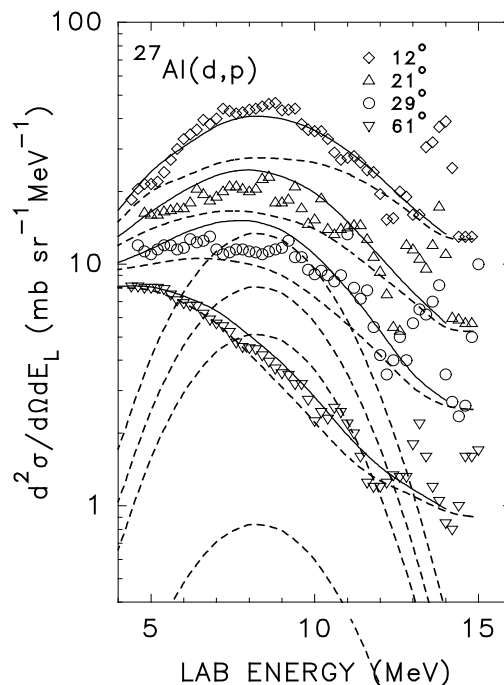
FIG. 11: Comparison of experimental and calculated double-differential breakup peaks for deuteron breakup on aluminum at 14.8 MeV. The points show the data from Ref. [1], the Gaussian-shaped dashed curves show the calculated breakup peaks, the other dashed lines show a reasonable estimate of the underlying cross section, and the solid curves show the total estimated spectra.

cross section. The most notable discrepancies are for aluminum, where the breakup cross section is particularly low; the 29 degree spectra from zirconium, where the calculations yield more intensity than the data; and the 51 degree results from tantalum, where the calculations yield less intensity. An interesting observation is that the spectra for the tantalum target, especially at 23 and 30 degrees, show signs of a second peak just slightly lower in energy than the breakup peak predicted by the general systematics. It is partly but not fully explained by the peak seen at backward angles, where breakup should be minimal, though it is possible that the contribution of this peak is greater at forward angles.

### B.   Deuteron breakup at 56 MeV

The data set at 56 MeV for $(d,p)$ breakup [5] is particularly useful because it comprises a large number of targets, includes angles down to 9.5 degrees, and uses an incident energy in a range of interest for the FENDL-3 database. Comparisons between calculation and experiment are shown in Figs. 15-19. The level of agreement here is, on average, significantly better than at 14.8 and 15 MeV, in part because the breakup cross section is higher, and in part because the dip at forward angles is not present as a complication. The results for the bismuth target show either a second peak at a slightly lower energy or a shoulder on the main breakup peak. This feature is not reproduced by the phenomenological model, and it's origin is not understood.

### VIII.   REMAINING WORK

Work is continuing to complete the comparisons between the model breakup peaks and the experimental double-differential cross sections in the present database. If the results continue to be satisfactory, the new model will be incorporated into the TUNL preequilibrium reaction code PRECO [12], and the absorbed (or non-observed) fragment will be allowed to initiate an equilibration process as described by the exciton model. Once that coding has been completed, a larger body of full energy spectra will be analyzed in order to complete the determination of the initial
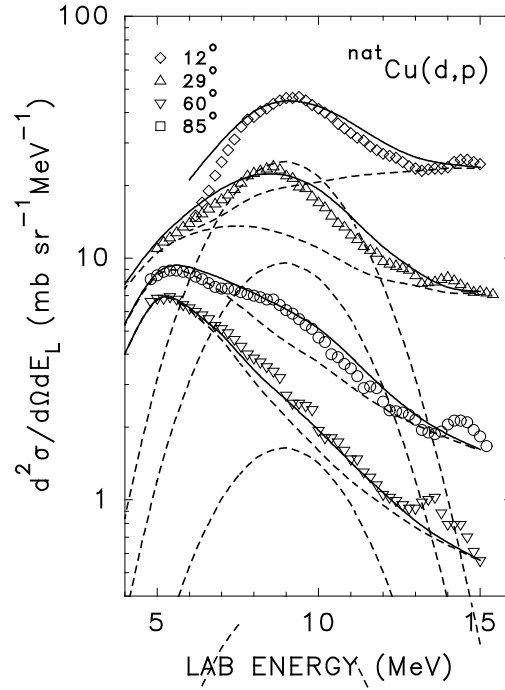
14



FIG. 12: Comparison of experimental and calculated double-differential breakup peaks for deuteron breakup on copper at 14.8 MeV. The points and curves have the same significance as in Fig. 11.
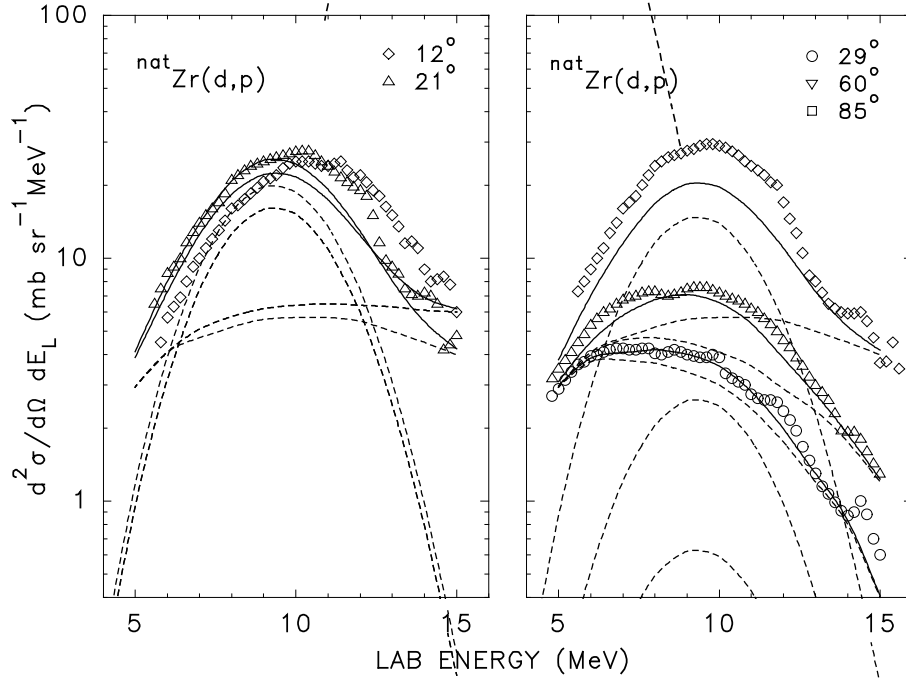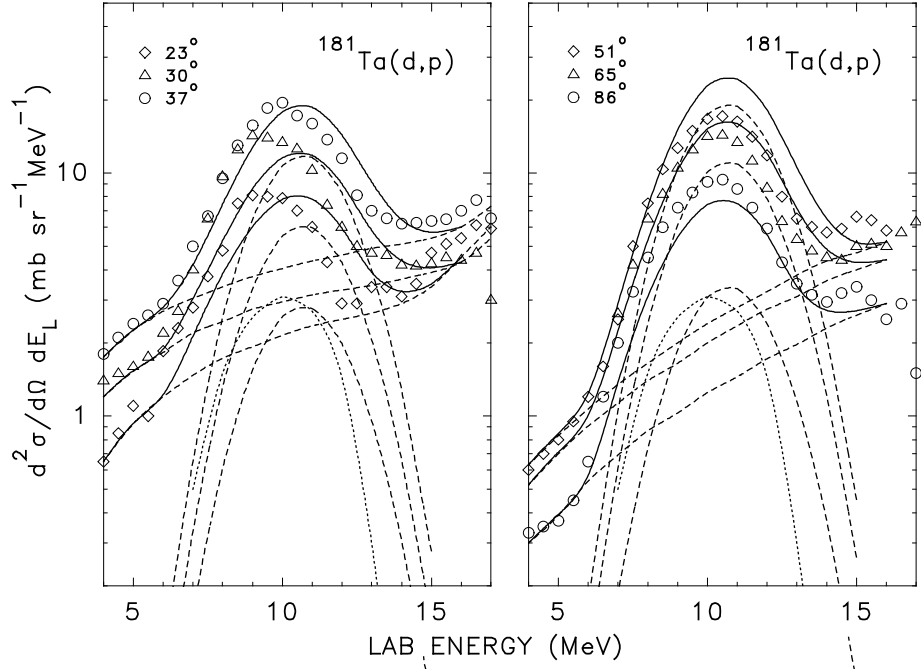


FIG. 13: Comparison of experimental and calculated double-differential breakup peaks for deuteron breakup on zirconium at 14.8 MeV. The points and curves have the same significance as in Fig. 11.
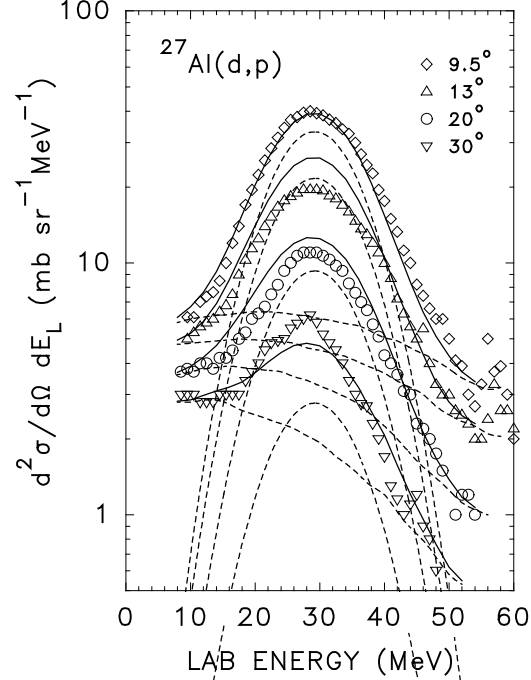
FIG. 14: Comparison of experimental and calculated double-differential breakup peaks for deuteron breakup on tantalum at 14.8 MeV. The points and curves have the same significance as in Fig. 11, except that the data are from Ref. [2], and the dotted curves show the background peak estimated from the 170 degree experimental spectrum, as discussed in the text. The data are actually in the center-of-mass system, but for such a heavy target the differences between the laboratory and center-of-mass systems is small.



FIG. 15: Comparison of experimental and calculated double-differential breakup peaks for deuteron breakup on $^{27}$Al at 56 MeV. The points show the data from Ref. [5], the Gaussian-shaped dashed curves show the calculated breakup peaks, the other dashed lines show a reasonable estimate of the underlying cross section, and the solid curves show the total estimated spectra.
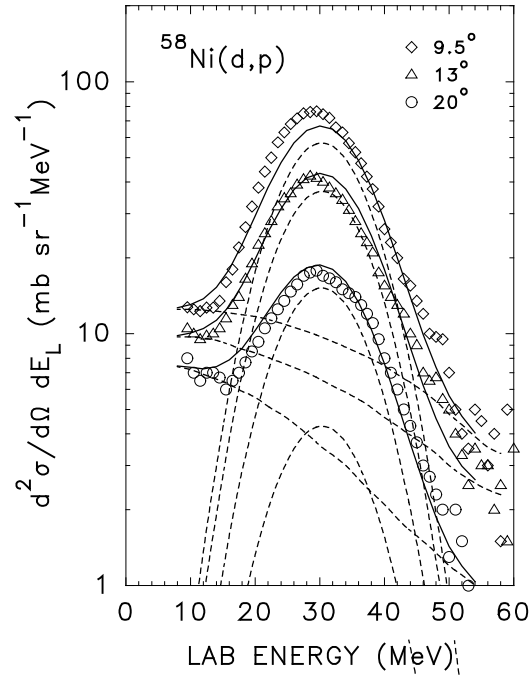
FIG. 16: Comparison of experimental and calculated double-differential breakup peaks for deuteron breakup on $^{58}$Ni at 56 MeV. The points and curves have the same significance as in Fig. 15.

particle-hole configuration in the exciton model for complex-particle-induced reactions.

[1] E. W. Hamburger, B. L. Cohen, and R. E. Price, Phys. Rev., **121** (1961) 1143.
[2] J. Kleinfeller, J. Bisplinghoff, J. Ernst, T Mayer-Kuckuk, G. Baur, B. Hoffmann, R. Shyam, F. Rősel, and D. Trautman, Nucl. Phys., **A370** (1981) 205.
[3] J. Pampus, J. Bisplinghoff, J. Ernst, T. Mayer-Kuckuk, J. Rama Rao, G. Baur, F. Rősel, and D. Trautman, Nucl. Phys., **A311** (1978) 141.
[4] A. Chavarier, N. Chevarier, A. Demeyer, A. Alevra, I. R. Lukas, M. T. Magda, and M. E. Nistor, Nucl. Phys., **A237** (1975) 354.
[5] N. Matsuoka, M. Kondo, A. Shimizu, T. Saito, and S. Nagamachi, Nucl. Phys., **A345** (1980) 1.
[6] J. R. Wu, C. C. Chang, and H. D. Holmgren, Phys. Rev. C, **19** (1979) 370.
[7] N. Matsuoka, A. Shimizu, K. Hosono, T. Saito, M. Kondo, H. Sakaguchi, Y. Toba, A. Goto, and F. Ohtani, Nucl. Phys., **A311** (1978) 173.
[8] A. Djaloeis, J. Bojowald, S. Gopal, W. Oelert, N. G. Puttaswamy, P. Turek, and C. Mayer-Bŏricke, Phys. Rev. C, **27** (1983) 2389
[9] J. R. Wu, C. C. Chang, H. D. Holmgren, and R. W. Koontz, Phys. Rev. C, **20** (1979) 1284.
[10] J. R. Wu, C. C. Chang, and H. D. Holmgren, Phys. Rev. Lett., **40** (1978) 1013.
[11] R. W. Koontz, C. C. Chang, H. D. Holmgren, and J. R. Wu, Phys. Rev. Lett., **43** (1979) 1862.
[12] Constance Kalbach Walker, "Users Manual for PRECO-2006," unnumbered report, Triangle Universities Nuclear Laboratory, February 2007, available from the National Nuclear Data Center at Brookhaven National Laboratory, http://www.nndc.bnl.gov/nndcscr/model-codes/preco-2006/
[13] A. Chevarier, N. Chevarier, A. Demeyer, A. Alevra, R. Dumitrescu, I.R. Lukas, M.T. Magda, M.E. Nistor, Nucl. Phys., **A231** (1974) 64.
[14] A. M. Kalend, B. D. Anderson, A. R. Baldwin, R. Madey, J. W. Watson, C. C. Chang, H. D. Holmgren, R. W. Koontz, and J. R. Wu, Phys. Rev. C **28** (1983) 105.
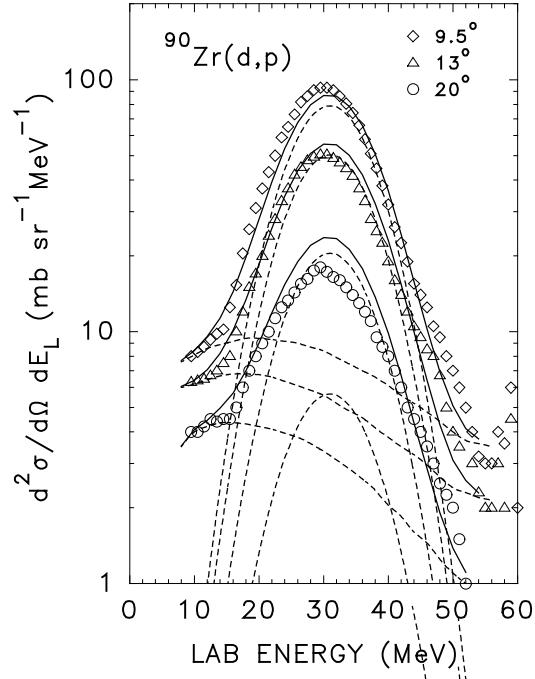
FIG. 17: Comparison of experimental and calculated double-differential breakup peaks for deuteron breakup on $^{90}$Zr at 56 MeV. The points and curves have the same significance as in Fig. 15.
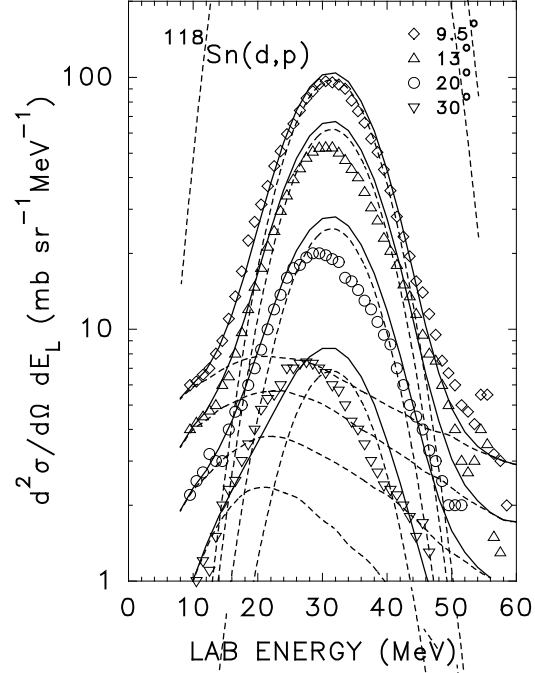


FIG. 18: Comparison of experimental and calculated double-differential breakup peaks for deuteron breakup on $^{118}$Sn at 56 MeV. The points and curves have the same significance as in Fig. 15.
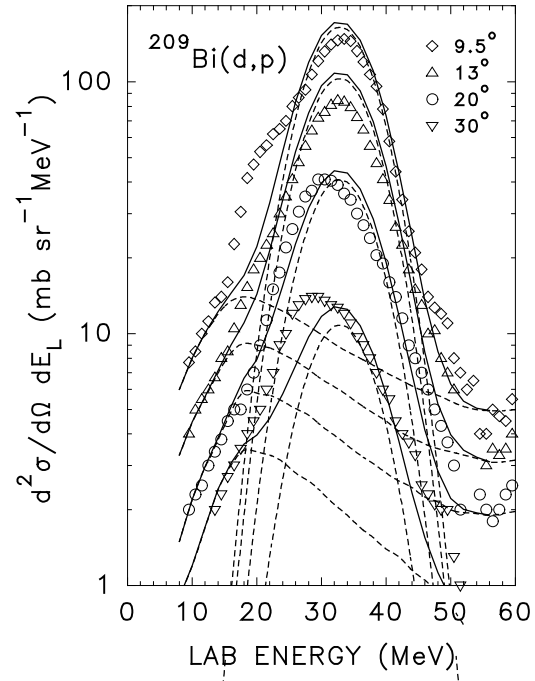
FIG. 19: Comparison of experimental and calculated double-differential breakup peaks for deuteron breakup on $^{209}$Bi at 56 MeV. The points and curves have the same significance as in Fig. 11.